48th AIAA/ASME/SAE/ASEE Joint Propulsion Conference & Exhibit
30 July - 01 August 2012, Atlanta, Georgia

AIAA 2012-3955

A fluiddynamic performance model of a helicon thruster

J. Navarro*, M. Merino† and E. Ahedo‡
Universidad Politécnica de Madrid, 28040 Madrid, Spain

A helicon thruster consists of a cylindrical helicon source, where the plasma is generated and heated, and a magnetic nozzle, where the plasma beam is accelerated supersonically. Two dimensional models of the plasma flow inside the source and in the external magnetic nozzle are derived, for a known amount of absorbed power from rf waves. 2D plasma structure and response inside the source are described, comprising the processes of neutral depletion, losses to chamber walls, and backward and forward flows. Conditions for high propellant utilization and high current efficiency are determined. The matching with the magnetic nozzle model yields the overall characterization of helicon thruster performances in terms of power, thrust and efficiency.

I. Introduction

Research in the helicon plasma thruster (HPT) carried out during last years suggests this kind of thruster as a candidate to gain a share in space propulsion. Different prototypes have been tested [1–4]. Opportunities in this challenge remain largely on the thrust efficiency figure. Recent studies [5,6] have measured the thrust of a low magnetic field HPT, obtaining a thrust efficiency below 5%. However, other authors [2, 3] claim that good thrust efficiency can be achieved. The possibility of operating with different propellants and the lack of electrodes are other valuable assets of the HPT. Otherwise, the complexity of the physics involved, plasma-wave interaction coupled with the flow dynamics of the magnetized plasma, has forced, so far, to analyze separately each physical process within the HPT.

Summarily, a helicon thruster, Fig. 1, can be divided into two parts: *(i)* the helicon source where plasma is produced (purple coloured) and *(ii)* the magnetic nozzle (MN) in which plasma is guided and accelerated (blue coloured). In the sketch and in the simulations presented later, a Maxwell coil set is used to generate the magnetic field in the source and in the MN. This kind of coils arrangement produces an almost constant ($\nabla |\mathbf{B}| \sim 0$) axial magnetic field along the dielectric tube (light green), that diverges smoothly downstream, forming the MN.

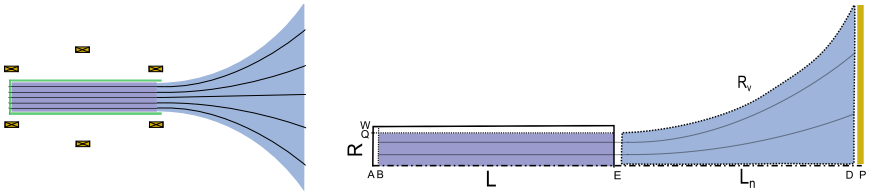

Figure 1. Helicon thruster sketch (left) and splitting into source and nozzle (right), labelling each part or main dimensions.

Inside the source, the plasma is quasineutral except at Debye sheaths, AB and QW, attached to the rear and lateral walls, respectively. At the source exit section E the plasma is assumed to flow sonically. Source and whole thruster efficiencies depend on the ionization degree reached inside the source. Along the

*PhD Student, jaume.navarro@upm.es, Full Adress: ETSI Aeronáuticos, Plaza Cardenal Cisneros, 28040 Madrid, Spain, Student AIAA Member.
†PhD Student, mario.merino@upm.es.
‡Professor, eduardo.ahedo@upm.es, Senior AIAA Member.

MN, from E until collecting plate P, the plasma beam is accelerated supersonically. As discussed later, the helicon thruster power balance, under the isothermal plasma hypothesis, requires to consider the whole cloud of confined electrons. For this reason and lacking a plasma detachment model, the conductive plate P has been included to close downstream the problem; a Debye sheath DP develops at the plate.

It is suitable to split the helicon thruster plasma physics in two mechanisms: *(i)* the plasma-wave interaction and *(ii)* the plasma flow dynamics. Regarding the first mechanism, an external antenna (not sketched in Fig. 1) is wrapped around the dielectric tube. This antenna emits RF waves which propagate within the plasma as helicon waves [7]. Thanks to plasma-wave interaction mechanisms, electromagnetic power is absorbed by the plasma [8–10]. The plasma-wave interaction process is not considered here: we will just assume that the plasma absorbs a power P_a from the rf emission. This work is devoted exclusively to study the plasma flow dynamics.

The previous description of HPT parts, points out the possibility of dividing the HPT fluid model into 'source' and 'magnetic nozzle' models. Furthermore, plasma properties in each sub-domain are different, allowing to assume different hypotheses. First, a 2D axisymmetric model of the source is derived following a variable-separation procedure in the radial and the axial direction. This technique was applied succesfully by Ahedo et al. [11] in a Hall thruster. Fruchtman et al. [12,13] where the first to apply it to a helicon source. Later, Ahedo [14] introduced several improvements and modifications in that model, such as: a 2D model of neutral depletion, a more consistent model of radial dynamics, an analytic solution of axial dynamics, and parametric studies of source performances.

Fruchtman et al. [12] proposed cleverly that the relation between the constant plasma temperature T_e and the absorbed power could be obtained from a global energy balance. However, they consider only the plasma source region for that balance. Here, we will show this to be inconsistent: the whole plasma region (i.e. source plus MN) needs to be considered for that balance. To achieve this purpose, the MN model of Ref. [15] is here matched with the source at section E. As commented before, plasma properties in the MN admit to modify partially some hypotheses. The MN model assumes the supersonic expansion of a collisionless, fully-ionized plasma. A slight mismatching between source and MN models might introduce a discontinuity in plasma properties at E. Nevertheless, if propellant utilization is high enough, the mismatching is small and overall performances in terms of thrust efficiency and power contributions are obtained.

The rest of the paper is organized as follows. Section II derives the helicon source fluid model. Then, sections III and IV provide, respectively, the plasma structure within the source and its performances. The matching between the source and the MN is presented in section V, in which overall thrust and power balances are carried out. Finally, main conclusions are summarized in section VI.

II. Helicon source plasma model

This model is basically the one derived in Ref. [14] so only a summary is presented here. An axisymmetric plasma is immersed in an axial magnetic field $\mathbf{B} = B\mathbf{1}_z$. The zero-Debye limit is invoked because plasma density is assumed high enough. Consequently, quasineutral plasma $n_e = n_i$ is assumed except in Debye sheaths. At the same time, plasma density is also low enough to assume the zero-beta limit, neglecting any induced magnetic field. Electrostatic sheaths, AB and WQ, are attached to the dielectric walls. Bohm criterion must be satisfied at sheath edges, B and Q. At the rear wall A, neutral gas $\dot{m}$ is injected and ionized due to collisions along the dielectric tube of length L and radius $R \ll L$.

Continuity and momentum equations, which describe the fluid-dynamic macroscopic behaviour of the plasma, are written down for the three species: ions (i), neutrals (n) and electrons (e),

$$\nabla \cdot (n_e \mathbf{u_e}) = \nabla \cdot (n_i \mathbf{u_i}) = -\nabla \cdot (n_n \mathbf{u_n}) = n_e n_n R_{ion}, \tag{1}$$

$$\nabla \cdot (m_j n_j \mathbf{u_j} \mathbf{u_j}) = -\nabla T_j n_j - q_j n \nabla \phi + q_j n_j \mathbf{u_j} \times \mathbf{B} - \mathbf{S_j}. \tag{2}$$

Here: n is the density; $\boldsymbol{u}$ is the velocity; m the mass of the particle; T the temperature of each specie; q is the electric charge; ϕ is the ambipolar electric potential; $\mathbf{S}_j$ includes momentum-transfer collisions, such as ionization (hereafter *ion* subscript) and elastic electron-ion (ei), ion-neutral (in), and electron-neutral (en) collisions; R_l ($l = ion, ei, in, en$) is the collisional rate of the different processes, and expressions are given in Appendix of Ref. [14].

Reference [14] explained the variable-separation method. The following hypotheses and conventions are made: electrons are isothermal; ion and neutral pressure are neglected; $\mathbf{u}_n = u_n \mathbf{1}_z$ and $n_n(r,z) = n_n(z)$;

there is local current ambipolarity, $\mathbf{j} - j_\theta \mathbf{1}_\theta = \mathbf{0}$; plasma density is decoupled as $n(z,r) = n_z(z) n_r(z,r)$, with $\int_0^R r n_r(z,r) dr = R^2/2$; the electric potential is decoupled as $\phi(z,r) = \phi_z(z) + \phi_r(z,r)$; and radial gradients are much higher than axial gradients. These assumptions lead to define axial and radial models coupled only through the wall-recombination function $S_w(z) \equiv n_z \nu_w(z)$, where $\nu_w(z)$ is the effective frequency of plasma recombination at the wall. As explained later, it is also the eigenvalue of the radial model. Next subsections present axial and radial models, listing equations that drive the behavior of the plasma.

A. Axial equations

The set of equations that control the axial behaviour along the dielectric tube becomes:

$$n_z u_z + n_n u_n = g_0, \tag{3}$$

$$(c_s^2 - u_z^2) \frac{\partial u_z}{\partial z} = (u_z - u_n) u_z n_n (R_{in} + R_{ion}) + c_s^2 (n_n R_{ion} - \nu_w), \tag{4}$$

$$(c_s^2 - u_z^2) \frac{\partial n_z}{\partial z} = -n_z \left[u_z \left(n_n R_{ion} - \nu_w \right) - \left(u_z - u_n \right) n_n \left(R_{in} + R_{ion} \right) \right], \tag{5}$$

$$n_n u_n \frac{\partial u_n}{\partial z} = n_z \left[u_n \nu_w \left(\alpha_w - 1 \right) + \left(u_z - u_n \right) n_n R_{in} \right]. \tag{6}$$

Here: g_0 the mass flux, $c_s = \sqrt{T_e/m_i}$ the sonic velocity, α_w is an adjustable parameter that retains the momentum loss/gain due to recombination at the lateral wall. The set of equations is solved for n_z, u_z, n_n and u_n with the following boundary conditions,

$$u_{zB} = -c_s, \quad u_{zE} = c_s, \quad u_{nB} = u_{n0}, \quad g_0 \text{ known}; \tag{7}$$

u_{n0} is the neutral velocity at section B. The above equations yield that the main dimensionless parameters that controlling the axial behavior of the plasma are

$$L_* = c_s u_{n0} / R_{ion} g_0, \qquad R_{in}/R_{ion}, \qquad u_{n0}/c_s, \qquad \alpha_w. \tag{8}$$

The recombination parameter $\nu_w / n_n R_{ion}$ also controls the axial plasma response but it is determined by the radial model.

An analytical solution of the axial is found invoking the asymptotic limits of high magnetic confinement, $\nu_w / n_n R_{ion} \ll 1$, and low ion collisionality, $R_{in}/R_{ion} < u_{n0}/c_s \ll 1$. That solution is

$$u_n = u_{n0}, \qquad \frac{u_z}{c_s} = \tan\xi, \qquad \frac{c_s}{g_0} n_z = 2\eta_u \cos^2\xi, \qquad \frac{u_{n0}}{g_0} n_n = 1 - \eta_u \sin 2\xi, \tag{9}$$

$$\frac{z}{L_\star} = \int_{-\pi/4}^{\xi} \frac{1 - \tan^2 \xi'}{1 - \eta_u \sin 2\xi'} d\xi', \tag{10}$$

with $\eta_u = \dot{m}_{iE}/\dot{m}$ the propellant utilization, and ξ an auxiliary parameter in the interval $\xi \in (-\pi/4, \pi/4)$.

B. Radial equations

The radial model was extensively discussed in Ref. [16]. Main equations are

$$\frac{1}{r} \frac{\partial}{\partial r} \left(r n_r u_r \right) = n_r \nu_w, \tag{11}$$

$$u_r \frac{\partial u_r}{\partial r} = -c_s^2 \frac{\partial \ln n_r}{\partial r} - \frac{eB}{m_i} u_\theta + \frac{m_e}{m_i} \frac{u_\theta^2}{r} - n_n \left(R_{in} + R_{ion} \right) u_r, \tag{12}$$

$$u_r \frac{\partial u_\theta}{\partial r} = \frac{eB}{m_e} u_r - \left[n_n (R_{en} + R_{ion}) + n R_{ei} \right] u_\theta - \frac{u_\theta u_r}{r}, \tag{13}$$

$$e \frac{\partial \phi_r}{\partial r} = T_e \frac{\partial \ln n_r}{\partial r} + eB u_\theta - m_e \frac{u_\theta^2}{r}. \tag{14}$$

Here, ν_w is the eigenvalue that assures the correct plasma flow balance. Equations are solved for n_r, u_r, $u_\theta \equiv u_{\theta e}$, and ϕ_r with the following homogeneous boundary conditions at the axis of symmetry,

$$u_r = u_\theta = \phi_r = \ln\left(n_r/n_r(z, r=0)\right) = 0. \tag{15}$$

Radial integration is carried out, in different cross-sections (i.e. different z), from the axis until the transition to the Debye-sheath Q. There, u_r must fulfill the Bohm criterion setting properly ν_w. The radial structure of the plasma is divided in three regions from the axis to the lateral wall. The bulk diffusive quasinetural region, a thin inertial layer where finite Larmour-radius effects cannot be neglected and the Debye sheath.

An analytic solution of the main, bulk region also exists. Here, the asymptotic limit is the high-magnetized regime $\omega_{lh} \gg \nu_e$. Moreover, the effective frequency of electron collisions $\nu_e = nR_{ei} + n_n R_{en} + n_n R_{ion}$ must be assumed radially constant $\nu_e = \text{const}$. Whereas in the complete model, ν_e varies radially due to $\nu_{ei} = n_r(z,r)R_{ei}$. This limit yields,

$$\frac{n_r(z,r)}{n_r(z,0)} = J_0\left(a_0 \frac{r}{R}\right), \quad \frac{u_r}{c_s} = a_0 \frac{\nu_e \omega_r}{\omega_{lh}^2} \frac{J_1\left(a_0 r/R\right)}{J_0\left(a_0 r/R\right)}, \quad \frac{u_\theta}{c_e} = \frac{u_r}{c_s}\frac{\omega_{lh}}{\nu_e}, \tag{16}$$

being $a_0 \simeq 2.405$ the first zero of Bessel function J_0, $c_e = \sqrt{T_e/m_e}$ the thermal electron velocity, and $\omega_r = c_s/R$ the radial transient frequency.

III. Plasma structure inside the source

This section shows main results of the 2D source model derived above. Axial, radial and 2D plasma structures are detailed. First of all, geometric and operational parameters are listed. The first group includes the tube length $L = 10$cm and its radius $R = 1$cm. On the other hand, operational parameters are the mass flow $\dot{m} = 0.1$mg/s, the plasma temperature $T_e = 10$eV, the neutral velocity $u_{n0} = 350$m/s and the magnetic field B. Two cases are studied: case 1 with $B = 200$G and case 2 with $B = 600$G. In both cases, all other parameters are maintained constant. $\alpha_w = 1$ is assumed here.

A. Axial response

Neutral depletion, Fig. 2(a), is governed by plasma ionization, $\nu_{ion} \propto n_n R_{ion}(T_e)$, and wall recombination ν_w. Higher temperatures and magnetic fields, and longer tubes improve the propellant utilization η_u. Plasma density, Fig. 2(b), presents a peak near $u_z \sim 0$ as indicated in Fig. 2(c). The positive gradient of the plasma density close to B is due to ionization; the negative gradient in the forward flow region is related to the plasma acceleration. Case 2 solution is almost indistinguishable from the analytical one (dashed line) because plasma parameters agree with asymptotic limit hypotheses. Otherwise, case 1 is more influenced by the role of wall losses in the plasma axial dynamics, Fig. 3(a), resulting in a worse correlation with the ideal-analytical solution.

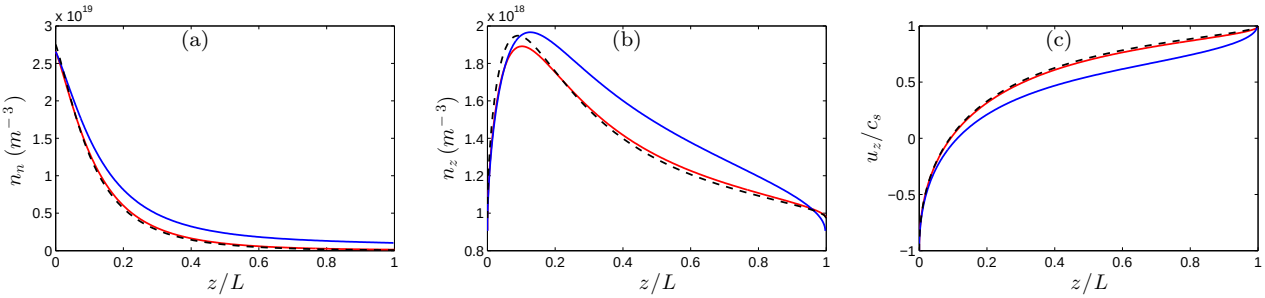

Figure 2. Blue solid line refers to the Case 1 (200G), red line refers to Case 2 (600G). The dashed line depicts asymptotic solution. This color-linestyle code is maintained in all other figures presented in this section. Fig. 2(a) depicts neutral depletion $n_n\,(m^{-3})$. Fig. 2(b) plots the plasma density axial profile $n_z\,(m^{-3})$. Plasma velocity response u_z/c_s is showed in Fig. 2(c).

Effective electron collisions ν_e, Fig. 3(b), which steer the plasma radial dynamics, decrease along the chamber, thus increasing radial magnetic confinement. Note that $\nu_e \sim \nu_{en}(z)$ near B and $\nu_e \sim \nu_{ei}(z,r)$ near

E. In other words, ν_e is dominated by electron-neutral collisions near B, where neutral density is still high, and this allows to assume that collisions are radially constant. On the other side, close to E, electron-ion collisions dominate. Consequently, the hypothesis of radially constant collisions cannot be assumed.

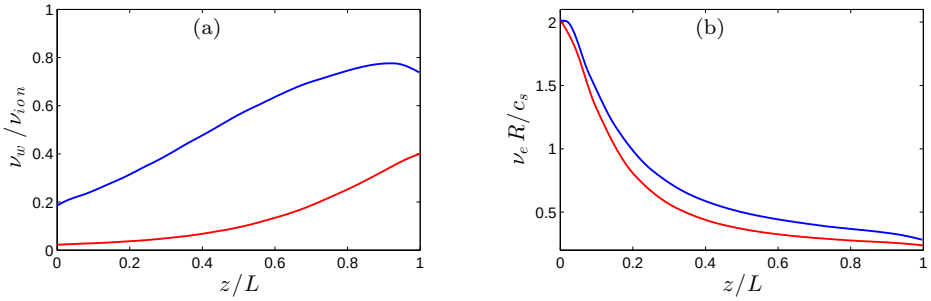

Figure 3. The role of wall losses is estimated in Fig. 3(a) in comparison with ionization rate ν_w/ν_{ion}. Fig. 3(b) depicts the axial variation of the dimensionless electron collisions frequency $\nu_e R/c_s$, necessary to estimate the radial magnetic confinement.

B. Radial response

Fig. 4(a) depicts plasma density profiles at the rear section B. There, case 2 is in agreement with the asymptotic solution proposed by Ref. [16], because both $\omega_{lh} = eB/\sqrt{m_e m_i} \gg \nu_e$ (highly-magnetized plasma) and $\nu_e(z,r) \sim \nu_{en}(z)$ (radially-constant collisions). Case 1 does not fulfil the analytical solution because $\omega_{lh} \sim \nu_e$. Fig. 4(b) refers to section E, where $\nu_e(r) \sim \nu_{ei}(r) \propto n_r$ makes these profiles more steepened. Profiles of $u_r(r)$ in Fig. 5(a) illustrate the high magnetic confinement of the plasma. Taking into account that $-e\phi \sim m_i u_r^2/2$, last results point out that radial electric field is only important in a thin inertial layer preceding the Debye sheath. $u_\theta(r)$ develops thanks to collisions, Fig. 5(b). The azimuthal plasma current provides the magnetic force that sustains the large radial density drop as in a θ-pinch.

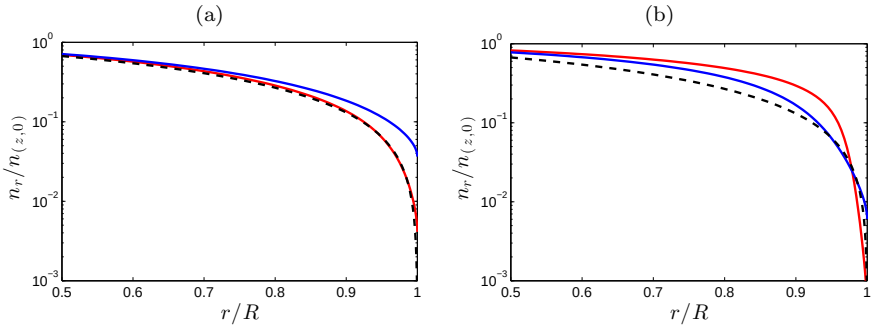

Figure 4. Fig. 4(a) depicts the plasma density radial profile in a cross section located at the rear part of the tube, close to B. The same property is shown in a section close to E, Fig. 4(b). Profiles are dimensionless, using as a reference value the density at the axis line $(z, r = 0)$

C. 2D density distribution in the helicon source

A 2D map of the plasma density is presented in Fig. 6. It is the natural response of the 200G case. Large gradients of the plasma density appear close to all walls. Radial gradients increase with magnetic confinement, in fact with the effective Hall parameter ω_{lh}/ν_e. Axial gradients close to A/B are due to electrostatic confinement and drive the backstreaming flow, which has been depicted in Fig. 2(c).

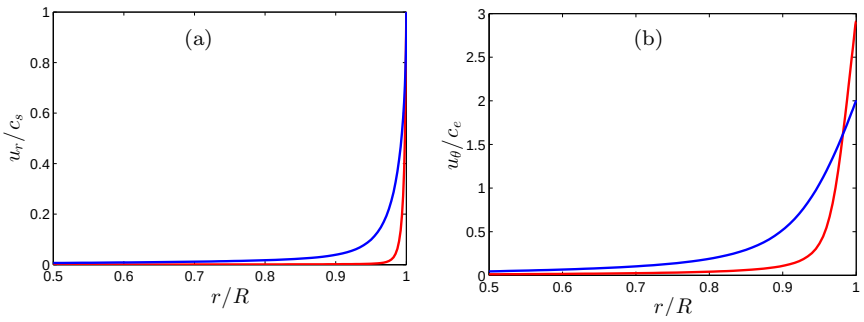

Figure 5. Fig. 5(a) plots the radial velocity u_r/c_s. Fig. 5(b) shows the radial profile of the electron azimuthal velocity.

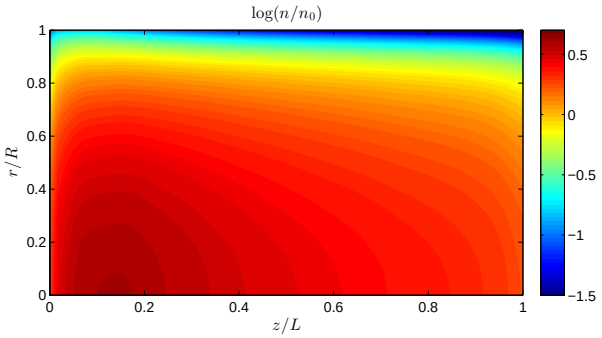

Figure 6. 2D plasma density distribution

IV. Source Performances

Assessment of the helicon source efficiencies is carried out in terms of the propellant utilization η_u and the production efficiency η_p,

$$\eta_u = \frac{\dot{m}_{iE}}{\dot{m}}, \tag{17}$$

$$\eta_p = \frac{\dot{m}_{iE}}{\dot{m}_{iA} + \dot{m}_{iW} + \dot{m}_{iE}}. \tag{18}$$

Propellant utilization measures the amount of ionized gas ejected through the exit section E relative to the injected mass flow. On the other hand, production efficiency compares the ionized gas flowing through E relative to the total amount of ionized gas produced inside the source.

Eq. (10), derived in the axial analytical model, states that η_u increases with T_e, L and $\dot{m}$. High efficiencies $\eta_u > 0.95$ require $L_* > 2.5$ as shown in Fig. 7(a). Figure 7(b) plots $\eta_u - B$ curves for different electron temperatures. The knee of each η_u curve separates low-utilization regimes (low-magnetized plasmas) from the high-utilization regimes. Note also, even for very high magnetic field intensities, high-utilization regimes are limited by the plasma temperature, noticeable in the case $T_e = 7\,eV$, in which ionization is compensated by wall losses, limiting the maximum η_u available. Fig. 7(c) indicates that the flow to the rear wall should be reduced because it represents almost 50% of η_p losses. If a perfect magnetic screening is assumed at the rear wall, η_p may reach values over 90% within the typical range of magnetic field intensities $500 - 1000$G.

V. Matching with the magnetic nozzle

The source model matches the 2D MN model of Ahedo and Merino [15], which provides the supersonic plasma expansion. Currents developed at the plasma plume are closed at P, where ϕ_P =const. This

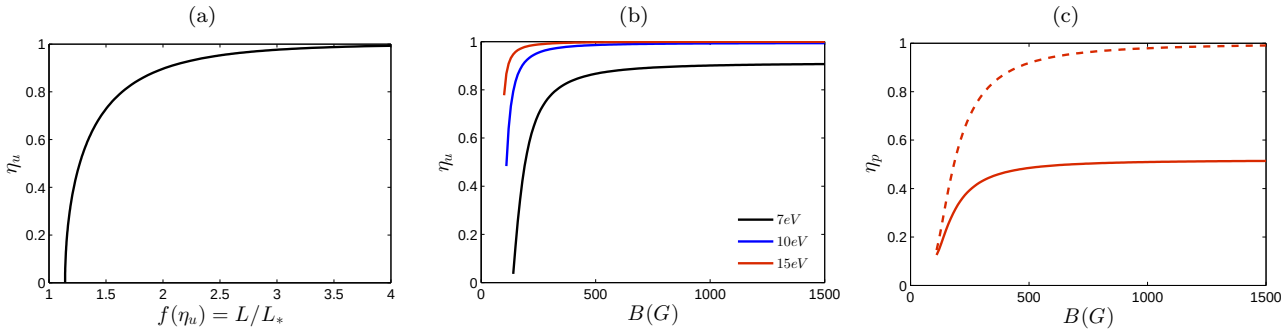

Figure 7. Fig. 7(a) plots the law of Eq. (10). Propellant utilization as a function of the magnetic field is depicted in Fig. 7(b) for different values of the electron temperature. Fig. 7(c) shows the differences on the production efficiency if the backstreaming flow is neglected (dashed line) thanks to an hypothetical screening system (This example uses the Case 2, 600G, as the reference case, solid line).

potential is solved from a fluid-kinetic formulation at the sheath transition D. MN model hypotheses have been commented partially in Sec. I. Other essential hypotheses are listed next. This fluid model of the plasma expansion assumes: *(i)* fully-magnetized electrons whereas ions are partially-magnetized; *(ii)* the plasma is current free; *(iii)* current ambipolarity is not sustained within the plume. *(iv)* the flow at E must be parallel to the magnetic field streamlines; and *(v)* the ion Mach number slightly supersonic, in order to fulfill the requirements of the hyperbolic MN model.

Taking into account all hypothesis enumerated above, only the bulk region $r/R \leq 0.98$ of the plasma flowing through E is considered. It supposes a small mismatching in the continuity, momentum and energy laws. The error committed is smaller than 5%. The plasma density distribution along the complete device is depicted in Fig. 8. It shows how density varies much less inside the source than in the plume, where it may drop up to 4 orders of magnitude, presenting a high *radial rarefaction*.

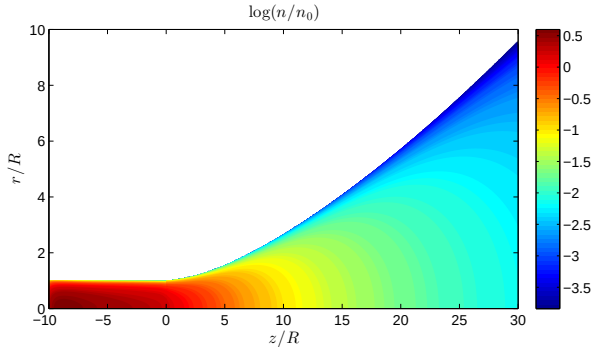

Figure 8. 2D map of the plasma density in the whole thruster $\log(n/n_0)$. Case 1 - 200G. Plasma density reference defined as $n_0 = g_0/c_s$.

After obtaining MN results it is possible to evaluate both the power balance and the total thrust, as well as partial contributions to this thrust. Next subsections presents these balances.

A. Energy balance

Energy balance in the whole thruster determines the relation between the absorbed power P_a, the constant temperature of the electron cloud, and the length L_n of the MN region. Obtaining an implicit law $P_a = P_a(T_e, L_n)$ as Fig. 9(a) illustrates. The most general form of the energy equation, grouping all contributions of all species becomes

$$\nabla \cdot \dot{\boldsymbol{P}} = \boldsymbol{j} \cdot \boldsymbol{E} + \dot{P}_a - \dot{P}_{ion}, \tag{19}$$

where

$$\dot{\boldsymbol{P}}(z,r) = \frac{n_n}{2} m_i u_n^2 \boldsymbol{u}_n + \frac{n}{2}\left[m_i u_i^2 \boldsymbol{u}_i + (m_e u_{\theta e}^2 + 5T_e)\boldsymbol{u}_e\right] + \boldsymbol{q}_e, \tag{20}$$

$\mathbf{q_e}$ is the heat flux, $\boldsymbol{j} \cdot \boldsymbol{E}$ is the electric field work, $\dot{P}_a$ the absorbed power density, and $\dot{P}_{ion}$ is the the power density for ionization and excitation processes, defined as

$$\dot{P}_{ion} = E'_{ion} n n_n R_{ion} \equiv \nabla \cdot (E'_{ion} n \boldsymbol{u}_i), \tag{21}$$

with E'_{ion} the effective ionization energy (see Appendix of Ref. [14]).

Equation (19) can be easily integrate over the whole domain, yielding

$$P_{ion} + P_{wall} + P_P = P_a. \tag{22}$$

where P_a is the absorbed power from the wave, P_{ion} groups ionization and excitation energy losses, $P_{wall} = P_A + P_W$ groups losses at tube rear wall A and lateral wall W, and P_P is the plasma power impacting at plate P. The three magnitudes on the left-hand side on Eq. (22) depend on T_e; additionally, P_P *depends on the length* L_n *of the MN region.*

If T_e = const, P_a increases as MN length is extended, because P_P rises monotonically in this MN isothermal model. Reciprocally, T_e decreases for longer MN and P_a = const. At $L_n = 0$ (i.e. the plate is at the exit of the source), the difference between P_a, case 1, from that obtained in case 2, responds to the lower production efficiency of the source, penalized by wall losses and ionization of the recombined flux, $P_{wall} + P_{ion} \simeq 0.7 P_a$, see Fig. 9(b). Case 2 is shown as an efficient case, $P_P \simeq 0.40 P_a$. Ionization cost is similar in both cases $P_{ion}/P_a \sim 0.3$. The absorbed power obtained in these results belongs to the range $50 - 100W$. It is in accordance with experimental devices that use similar operational and geometric parameters, such as the one in Ref. [17].

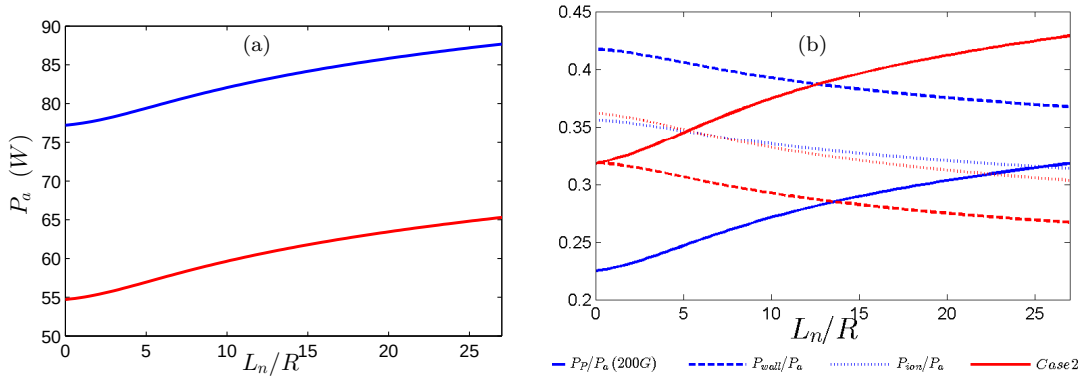

Figure 9. Fig. 9(a) plots the obtained power absorption law $P_a = P_a(L_n, T_e = 10eV)$. Fig. 9(b) shows the ratios P_P/P_a, P_{wall}/P_a and P_{ion}/P_a.

B. Thrust balance

Finally, regarding the thrust balance, this research focuses the effort on breaking down all contributions to the total thrust F,

$$F = F_{pres} + F_{elec} + F_{mag}. \tag{23}$$

As Eq. 23 indicates, three contributions can be taken into account. First, F_{pres} includes the thrust due to the pressure on the helicon source walls, mainly at the rear section A. Moreover, a small negative contribution is due to the loss of momentum at the lateral wall as a consequence of plasma-wall recombination. The second term, F_{elec} is the electric force between the negative electric charge at surface A and the positive electric charge at sheath AB. The third contribution, F_{mag}, comes from the thrust gain due to the MN, as a result of the interaction between azimuthal plasma currents and the magnetic circuit (i.e. applied divergent magnetic field).

Naturally, the thrust contributions are related to the axial momentum flow of the plasma at different sections z = constant, defined as

$$F_z(z) = 2\pi \int_0^{R_V(z)} dr r M_{zz}(z, r) \tag{24}$$

where $\mathbf{M} = \sum_{k=i,e,n} m_k n_k \mathbf{u}_k \mathbf{u}_k + p_e \mathbf{I}$ is the plasma momentum flux tensor. From this definition, it is possible to relate each contribution in Eq. (23) with the axial momentum flow evaluated at sections E and D,

$$F_{zE} = F_{pres} + F_{elec}, \tag{25}$$

$$F_{zD} = F. \tag{26}$$

Therefore, $F_{mag} = F_{zD} - F_{zE}$. Finally, with the computed thrust $F = F(L_n, T_e)$ and the absorbed power, the thrust efficiency η is defined as follows,

$$\eta = \frac{F^2}{2\dot{m}P_a}. \tag{27}$$

Figure 10 plots $\eta = \eta(L_n, T_e = 10eV)$. In the highly-magnetized case (600G) thrust efficiency is over 20% if $L_n/R \geq 14$.

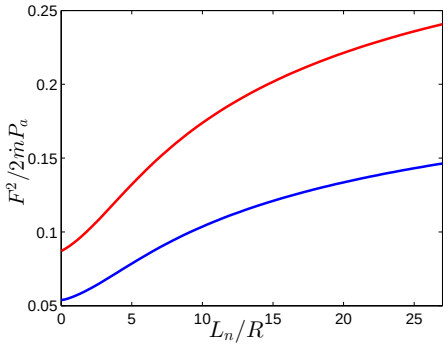

Figure 10. Source + MN thrust efficiency η

VI. Conclusions

A 2D fluid model of the helicon source has been derived and matched to a similar model of the magnetic nozzle. Attention has been given to the 2D neutral depletion and the plasma confinement from rear and lateral walls of the source. Source performances are given in terms of the propellant utilization and production efficiency. Ranges of design and operational parameters for optimal performances are identified. Analytic solutions compare well with numerical solutions within appropriate parametric ranges.

The matching of the source model with a divergent MN model has allowed the first complete characterization of the plasma discharge in a helicon plasma thruster. Additionally, it has allowed to solve a previous inconsistency in relating the plasma temperature with the absorbed power, which turns out to involve the plasma expansion in the MN. The different contributions to the thrust and the energy balance have been analyzed. Encouraging values of the thrust efficiency are obtained.

Further work should try to couple this plasma flow model with a 2D model of the plasma-wave interaction, in order to ascertain the validity of the assumptions made in the flow model here or how they should be modified. For instance, a non-Maxwellian distribution function of electrons could modify the results. Also, a downstream plasma detachment model would allow us to avoid the downstream plate included here.

Acknowledgments

This work has been supported by the Spanish Government (Project AYA-2010-61699) and the Air Force Office of Scientific Research, Air Force Material Command, USAF (grant FA8655-12-1-2043). The U.S Government is authorized to reproduce and distribute reprints for Governmental purpose notwithstanding any copyright notation thereon.

References

[1]Pavarin, D., Manente, M., Guçlua, Y., Curreli, D., Bettanini, C., Zaccariotto, M., Walker, M., Palmer, D., Carlsson, J., Bramanti, C., et al., "Feasibility Study of Medium-Power Helicon Thruster," *44th AIAA/ASME/SAE/ASEE Joint Propulsion Conference & Exhibit*, 2008.

[2]Ziemba, T., Carscadden, J., Slough, J., Prager, J., and Winglee, R., "High Power Helicon Thruster," *41th Joint Propulsion Conference, Tucson, AR*, edited by A. I. of Aeronautics and W. Astronautics, AIAA 2005-4119, 2005.

[3]Batishchev, O., "Minihelicon Plasma Thruster," *IEEE Transaction on Plasma Science*, Vol. 37, 2009, pp. 1563–1571.

[4]Lafleur, T., Charles, C., and Boswell, R., "Characterization of a helicon plasma source in low diverging magnetic fields," *Journal of Physics D: Applied Physics*, Vol. 44, 2011, pp. 055202.

[5]Takahashi, K., Lafleur, T., Charles, C., Alexander, P., Boswell, R., Perren, M., Laine, R., Pottinger, S., Lappas, V., Harle, T., et al., "Direct thrust measurement of a permanent magnet helicon double layer thruster," *Applied Physics Letters*, Vol. 98, 2011, pp. 141503.

[6]Ling, J., West, M., Lafleur, T., Charles, C., and Boswell, R., "Thrust measurements in a low-magnetic field high-density mode in the helicon double layer thruster," *Journal of Physics D: Applied Physics*, Vol. 43, 2010, pp. 305203.

[7]Boswell, R., "Very efficient plasma generation by whistler waves near the lower hybrid frequency," *Plasma Physics and Controlled Fusion*, Vol. 26, 1984, pp. 1147–1162.

[8]Chen, F., "Plasma ionization by helicon waves," *Plasma Physics and Controlled Fusion*, Vol. 33, 1991, pp. 339.

[9]Shamrai, K. and Taranov, V., "Resonance wave discharge and collisional energy absorption in helicon plasma source," *Plasma Physics and Controlled Fusion*, Vol. 36, 1994, pp. 1719–1735.

[10]Lieberman, M. and Lichtenberg, A., *Principles of plasma discharges and materials processing*, Wiley-Blackwell, 2005.

[11]Ahedo, E., Gallardo, J., and Martínez-Sánchez, M., "Effects of the radial-plasma wall interaction on the axial Hall thruster discharge," *Physics of Plasmas*, Vol. 10, No. 8, 2003, pp. 3397–3409.

[12]Fruchtman, A., Makrinich, G., and Ashkenazy, J., "Two-dimensional equilibrium of a low temperature magnetized plasma," *Plasma Sources Science and Technology*, Vol. 14, 2005, pp. 152–167.

[13]Fruchtman, A., "Neutral depletion in a collisionless plasma," *Plasma Science, IEEE Transactions on*, Vol. 36, No. 2, 2008, pp. 403–413.

[14]Ahedo, E., "Cylindrical model of a helicon-generated plasma," *31th International Electric Propulsion Conference, Ann Arbor, Michigan, USA*, edited by F. Electric Rocket Propulsion Society, IEPC 2009-193, 2009.

[15]Ahedo, E. and Merino, M., "Two-dimensional supersonic plasma acceleration in a magnetic nozzle," *Physics of Plasmas*, Vol. 17, 2010, pp. 073501.

[16]Ahedo, E., "Parametric analysis of a magnetized cylindrical plasma," *Physics of Plasmas*, Vol. 16, 2009, pp. 113503.

[17]Pavarin, D., Ferri, F., Manente, M., Curreli, D., Guclu, Y., Melazzi, D., Rondini, D., Suman, S., Carlsson, J., Bramanti, C., Ahedo, E., Lancellotti, V., Katsonis, K., and Markelov, G., "Design of 50W Helicon Plasma Thruster," *31th International Electric Propulsion Conference, Ann Arbor, Michigan, USA*, edited by F. Electric Rocket Propulsion Society, IEPC 2009-205, 2009.